Efficient Representation and Optimization of TPMS-Based Porous Structures for 3D Heat Dissipation☆

Shengfa Wang [a],[*], Yu Jiang [a], Jiangbei Hu [a], Xin Fan [a], Zhongxuan Luo [a], Yongjin Liu [b], Ligang Liu [c]

[a] *Dalian University of Technology, China*
[b] *Tsinghua University, China*
[c] *University of Science and Technology of China, China*

ARTICLE INFO

ABSTRACT

Triply periodic minimal surfaces (TPMSs) have been widely used in many engineering fields, including tissue engineering, lightweight manufacturing, and biomedicine. Although TPMSs have many nice properties that make them very suitable for thermal property analysis, there has been little work that has applied TPMSs in this important field due to the high complexity of representation and optimization. This paper presents an efficient representation and optimization of TPMS-based porous structures for heat dissipation. First, the porous structure is established by a function representation that is derived by the function representations of TPMSs. It inherits the good properties of TPMSs, such as high surface-to-volume ratio, full connectivity, high smoothness, and controllability. Then, according to the steady-state heat conduction equation, the heat dissipation problem can be formulated into a minimization problem dealing with the mean temperature distribution using the given constraints. Next, to solve the problem directly on function representation without remeshing, an efficient optimization method with global–local interpolation is exploited. Finally, we obtain the optimized porous shell structures with smooth period and wall-thickness changes. Different from traditional TPMS-based methods, the proposed approach provides both efficient function representation and optimization of TPMS-based porous shell structures for heat dissipation. Various experiments were conducted showing that the proposed porous structures have obvious advantages in terms of efficiency and effectiveness.

1. Introduction

How to construct lightweight and efficient structures for heat dissipation has received considerable attention in various engineering fields. The traditional heat sink structures cannot achieve high thermal conduction efficiency. Porous structures have been explored for solving this problem, and they could efficiently promote thermal conduction. However, representation and optimization become technical bottlenecks that limit their further development. It is difficult for the traditional structure design for heat dissipation, depending on the basic theory of heat transfer and practical experience, to solve the heat transfer problems on complex structures. Later, topology optimizations of porous structures, such as tree-like topology structure, truss/frame structures, and micro-structures, were exploited to handle the above

problems [1–4]. These porous structures can be used to calculate the high degree of freedom of the cooling channel topology configuration. However, these approaches share a common problem that they have many of design variables and the optimization is costly due to time-consuming remeshing.

Recently, TPMS-based porous structures have been widely applied in tissue engineering technology, lightweight manufacturing, biomedicine, and other fields [5–7]. The TPMS-based porous structures have various superiorities in generation and applications, such as perfect inter-connectivity, ease of and precise controllability, high surface-to-volume ratio, and high specific strength and stiffness to relatively low mass. Furthermore, porous surfaces can be expressed by implicit functions, and they can be easily controlled by period and wall-thickness parameters. Therefore, they have been successfully used for engineering porous scaffold designs. There are many publications of TPMSs, but most of them represented TPMS-based shell structures (with thickness) by discrete polyhedron mesh (tetrahedron or hexahedron), which is extremely time and memory-consuming in optimization,

especially for large and complex porous structures. Moreover, the traditional FEM-based processing methods of TPMS-based porous structures are mostly heuristic methods without efficient optimization. Due to the complexity of representation and optimization, there has been little work on TPMS-based porous structures on heat dissipation.

In this paper, efficient representation and optimization are exploited to obtain the proper period and wall-thickness of TPMS-based porous shell structures for heat dissipation. The structure is constructed by two parameter functions to dominate the porous period and the wall thickness, respectively. The optimization is efficient, because the calculations of integral and gradient can be directly implemented on these functions without remeshing, and only simple uniform voxel elements are constructed once, to serve as the background integration domain. As shown in Fig. 1, the main optimization process consists of the period optimization and wall-thickness optimization. The former is considered to be a coarse adjustment on the structure while the latter is considered a fine adjustment on the structure. First, the porous shell structures are expressed by implicit function, which is controlled by two parameter functions, including the period parameter function and the wall-thickness parameter function. Based on these, the steady-state heat conduction equation with boundary conditions can be easily built into a mathematical model directly using a function representation. Then, to solve above two continuous parameter functions, the optimization of the model can be transferred to few control points. From the viewpoint of discretization, the two parameter functions can also be efficiently calculated using the distance field constructed by the implicit function without remeshing. As a result, the optimized porous structures with smooth period and wall-thickness changes are obtained. The main contributions of this work can be summarized as follows:

1. We derive a novel representation of TPMS-based porous shell structure with two control functions, which independently dominate the periodic holes and wall-thickness of porous structures, respectively. The proposed porous structures also inherit several good properties of TPMS, such as high surface-to-volume ratio, smoothness, and controllability.
2. We present a two-step optimization scheme that can be directly executed on the function representation of TPMS-based porous structures for heat dissipation. Moreover, the porous structures can be analyzed and optimized directly on function representation without time-consuming remeshing.
3. We adopt the optimization method with a global–local interpolation to accelerate the efficiency of solving the problem of steady-state heat conduction. Various experiments certified the efficiency and effectiveness of the proposed method.

2. Related work

Common structural optimization for heat dissipation. There are several structural optimization methods for the heat transfer problem, such as element-based method, explicit method and composite method for multi-scale optimization. For the element-based methods, homogenization methods [8,9], solid isotropic material with penalization (SIMP) methods [10,11] and evolutionary structural optimization (ESO) methods [12,13] are commonly used in the design of heat dissipation structures. Bendsøe and Sigmund [14] directly extended the density method in structural topological optimization to the heat transfer structure optimization and studied simple steady-state heat conduction using a two-dimensional (2D) finite element framework. Gersborg-Hansen

et al. [15] solved the planar heat conduction problem through a finite volume method combined with SIMP method. Page et al. [16] studied the two-dimensional numerical topology optimization of anisotropic materials based on the finite volume method and the SIMP method. Lin et al. [17] proposed a combination of traditional SIMP method and deep learning method to accelerate the topology optimization efficiency of two-dimensional heat conduction problems. Gao et al. [18] studied 2D conduction problems using an improved bi-directional ESO scheme. Li et al. [19] proposed an ESO method for the design of 2D heat conduction in the heat conduction field. Other element-based methods were also used in the design of 2D thermally conductive structures. Boichot et al. [20] attacked the conductive surface cooling problem by using a cellular automaton algorithm simulating the morphing by temperature gradients. Cheng et al. [21] realized bionic optimization in the construction of efficient thermal conduction paths by evolving the generation process and degeneration process of materials according to the temperature gradients. Another method for heat dissipation design is the explicit method, such as the level-set method [22,23] and component-based method [24,25]. Yamada et al. [26] proposed a mathematical model of topological optimization for heat transfer by maximizing thermal diffusion as the objective using a level-set method. Zhuang et al. [27] adopted a combination of the level set method and topological derivatives to solve the planar heat conduction problem, which considered a variety of load conditions. Bejan [24] put forward constructal-theory to solve the volumetric heat conduction problem. This method first optimized the initial units to obtain the dimensional parameters of the high heat conduction channel. Then, the assemblies were optimized step by step until the heat dissipation channel covers the required heat dissipation area. In addition, the composite method combines two or more topological methods in multi-scale topology optimization. Pizzolato et al. [28] proposed a multi-scale topology optimization model for multi-material structures, in which the structure, the layout of the material subdomains and their micro-structures are optimized concurrently. The macro-scale (the structure and the layout) is described by the level-set method, while the micro-scale (micro-structures) is represented by the SIMP method. However, most of the above methods were constructed in 2D cases, and it is difficult to directly extend them to 3D heat dissipation.

Some approaches have also been proposed for 3D thermal conduction. Dede [29], Chen et al. [1], Burger et al. [2] and Alexandersen et al. [30,31] considered the topology optimization of both two- and three-dimensional heat transfer, resulting in optimized topologies with tree features. However, the common problem of these approaches is that they implicitly perform structural optimization with many design variables, and it is costly to obtain precise solutions. Lohan et al. [32] used a generation algorithm that does not rely on the initial material distribution and grid to recursively generate 3D tree-like topology design. But the lack of self supports limits the scope of applications of the tree-like structures. Cheng et al. [3] exploited level set method to optimize a material density, then they mapped the density to obtain 3D lattice structure for thermal conduction. However, the method has limit on the solution accuracy and the structural flexibility, such as anisotropic variation. Moreover, explicit geometric methods, such as Moving Morphable Components (MMC) [33], had been success applied to solve problems with few parameters. Inspired by these work, we exploit more versatile and controllable TPMSs to construct porous structures for the thermal conduction. Then, an efficient optimization is adapted to solve the problem directly using functions without remeshing.
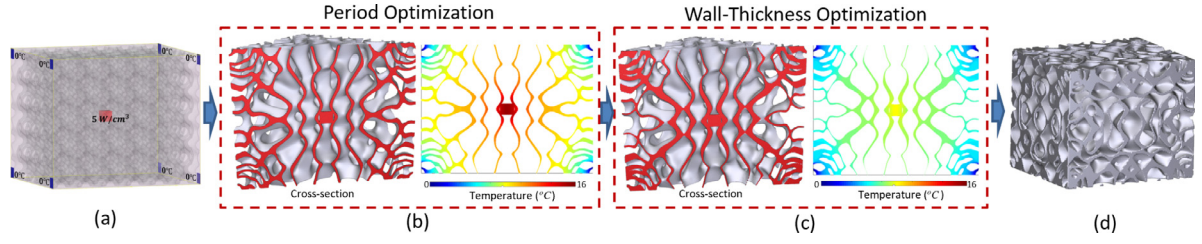
Fig. 1. Illustration of the optimization process for TPMS-based porous structures (P-TPMS). (a) Initial setting (red: heat source (50 W/m3); blue: cooling areas (0 °C)). (b) Cross-section of the 3D structure for period optimization and the corresponding temperature distribution in 2D (x = 1.2y plane). (c) Cross-section of the 3D structure for wall-thickness optimization and the corresponding temperature distribution. (d) Final optimized 3D porous structure. (For interpretation of the references to color in this figure legend, the reader is referred to the web version of this article.)

TPMS-based porous structures. TPMS-based structures have been widely studied in various fields [34]. Rajagopalan et al. [35] first attempted to apply TPMSs to construct Tissue engineering (TE) scaffolds. The advanced mechanical properties of the porous structures were demonstrated in mechanical and cell seeding tests. Melchels et al. [36] used K3DSurf software to generate the TPMS structures and construct dimensional gradient pores by adding a coefficient to the z value of the TPMS equation. They further explained that the mechanical properties of TPMS scaffolds can be controlled by the combination of materials and pore architecture. Yoo [37,38] proposed modeling algorithms using the volume distance field and thin-plate radial basis function, which made it easy to construct internal structures with smooth and natural changes. Cai and Xi [39] mapped TPMS structures to the designed shape by using coordinate interpolation and shape function of finite elements. Yang et al. [40] used the sigmoid function and Gaussian radial basis function to generate heterogeneous porous scaffolds. Hu et al. [41] improved the function of TPMSs by adding a parameter to control the period and offsetting the TPMS surface. But they did not provide an optimization of the structure, instead, they exploited a segmentation method to simplify the optimization at the cost of accuracy. Peng et al. [42] used the zero level set of TPMSs and the marching cube method to construct the porous structures. They applied the porous structures to heat dissipation analysis. However, they focused on the modeling and characterization of the TPMS-based porous structures but not the optimization of the porous structures. Ming et al. [43] proposed a porous solid structure constructed by extended triply periodic minimal surface for mechanical problems. But their method suffered from the lack of topology (porous period) optimization and a limited porosity of porous structures due to the design of their structures. Most of the above design and applications of the porous structures are simple and heuristic methods, which lead to undesired problems in structural optimization and controllability. Furthermore, using traditional FEM and heuristic methods to analyze and redesign porous structures is time-consuming and error-prone, especially for large objects. Due to the above problems, little work on TPMS-based porous structures has been devoted to solving the complex heat dissipation problem. Therefore, more efficient and controllable representation and optimization of TPMS-based porous structures is an urgent problem to be solved.

3. Construction of TPMS-based porous structures

TPMS. As minimal surfaces, the mean curvatures vanish at every point. There are some commonly used TPMS, including P-TPMS, G-TPMS, D-TPMS, and IWP-TPMS, and these TPMSs can also be approximated by the zero-level surfaces of trigonometric functions [34,36] as follows:

$$
\begin{aligned}
\varphi_P(\boldsymbol{r}) &= \cos(2\pi x) + \cos(2\pi y) + \cos(2\pi z) = 0, \\
\varphi_G(\boldsymbol{r}) &= \sin(2\pi x)\cos(2\pi y) + \sin(2\pi z)\cos(2\pi x) \\
&\quad + \sin(2\pi y)\cos(2\pi z) = 0, \\
\varphi_D(\boldsymbol{r}) &= \cos(2\pi x)\cos(2\pi y)\cos(2\pi z) \\
&\quad - \sin(2\pi x)\sin(2\pi y)\sin(2\pi z) = 0, \\
\varphi_{IWP}(\boldsymbol{r}) &= 2[\cos(2\pi x)\cos(2\pi y) + \cos(2\pi y)\cos(2\pi z) + \\
&\quad \cos(2\pi z)\cos(2\pi x)] - [\cos(2 \cdot 2\pi x) \\
&\quad + \cos(2 \cdot 2\pi y) + \cos(2 \cdot 2\pi z)] = 0,
\end{aligned}
\tag{1}
$$

where $\boldsymbol{r} = (x, y, z) \in \mathbb{R}^3$, x, y and z are the magnitudes in the Cartesian coordinate system. TPMSs have many beneficial properties, such as high surface-to-volume ratio, high smoothness, and fully inter-connectivity without enclosed hollows. It can be easy to control the periods and shapes of TPMSs by adjusting parameters. Moreover, TPMSs can also be used to construct porous structures, which have good mechanical properties and 3D manufacturability.

TPMS-based porous structures. TPMSs can be expressed by implicit functions. We propose a new function representation of TPMS-based porous structures by directly operating on implicit functions in a Signed Distance Field (SDF). The periodic holes (genus) and wall-thickness of the porous structures can be controlled by a period parameter function and a wall-thickness parameter function (distance bias), respectively. Moreover, the period and wall-thickness parameters are continuous parameter functions (period control function $P(\boldsymbol{r})$ and wall-thickness control function $W(\boldsymbol{r})$), which are used to control the changes of porous structures.

Given a type of TPMSs, the period control function $P(\boldsymbol{r})$ can be treated as a non-uniform scale of $\boldsymbol{r}$. $P(\boldsymbol{r})$ could be simply embedded into the function of the TPMS-based structures. However, this will cause value scaling (like scale transformation) in the SDF when the period function $P(\boldsymbol{r})$ changes. To eliminate the SDF scaling effect, we add a scale factor to the formulation that is defined as follows:

$$
\varphi^0(\boldsymbol{r}) = P(\boldsymbol{r}) \cdot \varphi\left(\frac{\boldsymbol{r}}{P(\boldsymbol{r})}\right) = 0.
\tag{2}
$$

Then, the wall-thickness of TPMS-based porous structures can be controlled using two surfaces that are offset from the above modified function by using the wall-thickness control function $W(\boldsymbol{r})$ as follows:

$$
\varphi^W(\boldsymbol{r}) = P(\boldsymbol{r}) \cdot \varphi\left(\frac{\boldsymbol{r}}{P(\boldsymbol{r})}\right) - W(\boldsymbol{r}) = 0,
\tag{3}
$$

$$
\varphi^{-W}(\boldsymbol{r}) = P(\boldsymbol{r}) \cdot \varphi\left(\frac{\boldsymbol{r}}{P(\boldsymbol{r})}\right) + W(\boldsymbol{r}) = 0.
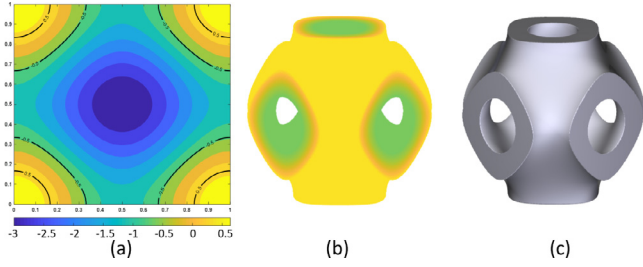\tag{4}
$$

Fig. 2. Construction of the TPMS-based porous structure (P-TPMS, $P(\mathbf{r}) \equiv 1$, $W(\mathbf{r}) \equiv 0.5$). (a) and (b) are the illustrations of the 2D SDF (middle face: z = 0.5 plane) and the 3D SDF, respectively. (c) is the corresponding 3D porous structure.

Fig. 3. Illustration of generic design domain.

Finally, the TPMS-based porous structures can be directly represented by these functions using disjunction operator as follows:

$$\Phi(\mathbf{r}) = -\varphi^W(\mathbf{r}) + \varphi^{-W}(\mathbf{r}) - \sqrt{\varphi^W(\mathbf{r})^2 + \varphi^{-W}(\mathbf{r})^2}, \tag{5}$$

where the region of $\Phi(\mathbf{r}) \geq 0$ represents a closed volumetric porous shell structure, as shown in Fig. 2. The function representation of TPMS-based porous structures inherits several good properties of TPMSs, including high surface-to-volume ratio, full connectivity, good smoothness, and high controllability. The high surface-to-volume ratio and full connectivity are excellent in terms of transferring heat. The high controllability provides directly computable optimization without remeshing for both period and wall-thickness. The good smoothness and connectivity are beneficial to 3D manufacturing because this guarantees the manufacturing accuracy and the leftover materials (such as the extra liquid in SLA) can be removed in 3D manufacturing.

4. Formulation of 3D heat dissipation

In this section, we formulate the 3D heat transfer problem using the proposed function representation of TPMS-based porous structures. In this approach, we mainly focus on the problem of steady-state heat conduction. Given a design domain, heat source, adiabatic, and temperature boundary conditions, this approach aims to obtain optimized TPMS-based porous structures with proper period and wall-thickness.

4.1. Steady-state heat conduction formulation

The general energy equation of steady-state heat conduction [2] can be expressed as follows:

$$\rho C_p \frac{\partial T}{\partial t} = \lambda \nabla^2 T + Q, \tag{6}$$

s.t.

$$T = \bar{T} \text{ on } \Gamma_T,$$
$$\lambda \frac{\partial T}{\partial n} = q_s \text{ on } \Gamma_Q,$$

where ρ is the material density, C_p is the specific heat, Q describes the internal heat generation term, $\lambda = (\lambda_x, \lambda_y, \lambda_z)$ is the material thermal conductivity in x, y, z directions, T is a temperature field, $\bar{T}$ is a given temperature on the Dirichlet boundary Γ_T, and q_s is the heat flux along boundary normal vector n of the Neumann boundary Γ_Q. For clarity, the heat conduction domain with boundary conditions is illustrated in Fig. 3.

The steady-state assumption ($\frac{\partial T}{\partial t} = 0$) is considered here, and the equation can be further simplified to an isotropic case by assuming $\lambda_x = \lambda_y = \lambda_z$. Thermal compliance is expressed in the form of thermal energy, and the optimization problem of
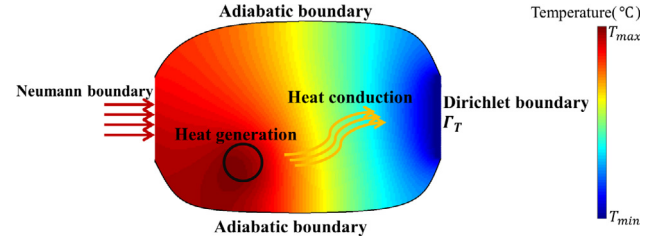
minimizing the thermal energy maximizes the structural thermal conducting efficiency. Therefore, the heat conduction problem in Eq. (6) can be rewritten using the Galerkin method [2] by adding volume and gradient constraints as follows:

$$\min_{P(\mathbf{r}), W(\mathbf{r})} C = \int_{\Gamma_Q} H(\Phi) q_S \cdot T d\Gamma + \int_{\Omega} Q \cdot T d\Omega \tag{7}$$

s.t.

$$a(\omega, T) = L(\omega) + B(\omega, \bar{T}),$$
$$V = \int_{\Omega} H(\Phi) d\Omega \leq \bar{v},$$
$$\| \nabla P(\mathbf{r}) \| \leq \bar{g},$$

where C ($W \cdot K$) is the thermal compliance to be minimized, which is the response of the structural temperature to external thermal loads (internal heat source loads and heat flow boundary). $a(\omega, T) = L(\omega) + B(\omega, \bar{T})$ is the weak solution formulation and the derivation of the formulation is shown in Appendix, V is the volume of the entire porous structure, $\bar{v}$ is the corresponding volume constraint, $\|\nabla P(\mathbf{r})\|$ is the gradient of the period function $P(\mathbf{r})$ (to obtain smooth porous changes, the gradient is used to control the degree of porous variation), $\bar{g}$ is the corresponding gradient constraint, and $H(x)$ is 0 when x is negative and 1 otherwise. In order to realize differentiable derivative calculation, the Heaviside function is updated to $H_\eta(x)$ [33]

$$H_\eta(x) = \begin{cases} 1, & \text{if } x > \eta, \\ \frac{3}{4}(\frac{x}{\eta} - \frac{x^3}{3\eta^3}) + \frac{1}{2}, & \text{if } -\eta \leq x \leq \eta, \\ 0, & \text{if } x < -\eta, \end{cases} \tag{8}$$

where η is the parameter that control the magnitude of regularization and the non-singularity of the global stiffness matrix, respectively. Moreover, for porous structures, the material thermal conductivity λ should be set to $\lambda = \frac{\lambda_S \cdot \lambda_D}{\delta \cdot (\lambda_D - \lambda_S) + \lambda_S}$, where δ is the volume ratio of solid material, λ_S and λ_D are the material thermal conductivity in the solid and void part, respectively.

4.2. Numerical implementation

The steady-state heat conduction equation with boundary conditions can be directly converted into a computable mathematical model based on the function representation of TPMS-based porous structures and the continuous control parameter functions $P(\mathbf{r})$ and $W(\mathbf{r})$. The optimization of the mathematical model can be transferred to solve the above two continuous parameter functions. In discrete calculation, the parameter functions can be efficiently solved using the SDF that was constructed by functions without remeshing. Only finite elements are needed to implement integral calculation, which makes the proposed optimization more efficient than traditional FEM-based optimizations.
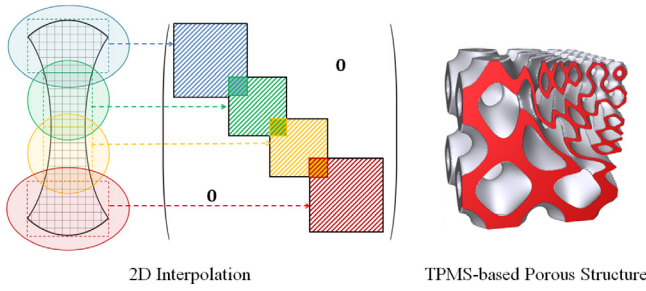
Fig. 4. Illustration of the global–local interpolation. (left) An example of a two-dimensional interpolation. (right) A TPMS-based Porous structure constructed using our global–local interpolation method. The period and wall-thickness of the structure change smoothly and naturally.

4.2.1. Global–local interpolation

The calculation of continuous parameter functions can be transferred into an optimization with a finite number of design variables by using radial basis interpolation [44]. A global–local representation of the RBF interpolation is proposed to reduce the complexity of calculation. The key idea of the local interpolation is to divide the large coefficient matrix into smaller coefficient matrices with weights.

Taking the period parameter $P(\boldsymbol{r})$ for an example. Ω is first divided into n_l finite sub-domains $\{\Omega_i\}_{i=1}^{n_l}$ ($n_l = 8$ by default). The period function can be approximated by the local functions obtained by the radial basis interpolation in local ellipsoids (containing the corresponding sub-domains) as follows:

$$P(\boldsymbol{r}) = \sum_{k=1}^{n_l} \frac{\omega_k(\boldsymbol{r})}{\sum_{j=1}^{n_l} \omega_j(\boldsymbol{r})} \cdot P_k(\boldsymbol{r}) = \sum_{k=1}^{n_l} \psi_k(\boldsymbol{r}) \cdot P_k(\boldsymbol{r}), \quad (9)$$

$$\omega_k(\boldsymbol{r}) = \left(\frac{(R_k(\boldsymbol{r}) - d_k(\boldsymbol{r}))_+}{(R_k(\boldsymbol{r}) \cdot d_k(\boldsymbol{r}))} \right)^2,$$

where $\psi_k(\boldsymbol{r})$ is the weight coefficient defined by $\omega_k(\boldsymbol{r})$, $d_k(\boldsymbol{r}) = \|\boldsymbol{r} - C_k\|_2$ is the distance from interpolation point to the center point C_k of an ellipsoid. The radial basis based on ellipsoid corresponds to the cuboid subregion, while its common case (Gaussian radial basis, etc.) corresponds to the cube subregion. $(*)_+$ is a truncation function satisfied if $x > 0$, $(x)_+ = x$, otherwise $(x)_+ = 0$, and $R_k(\boldsymbol{r})$ is a local interpolation of the period parameter in the kth sub-domain Ω_k defined as

$$P_k(\boldsymbol{r}) = \sum_{j=1}^{n_{kt}} R_{ki}(\boldsymbol{r}) a_{ki} + \sum_{j=1}^{m} q_{kj}(\boldsymbol{r}) b_{kj}, \quad (10)$$

where $R_{ki}(\boldsymbol{r}) = (\boldsymbol{r} - O_{ki})^2 log(|\boldsymbol{r} - O_{ki}|)$ is the logarithmic radial basis function with $R(x) = x^2 log(|x|)$, $\{O_{ki}\}_{h=1}^{n_{kt}}$ are the control points in the sub-domain Ω_k, n_{kt} is the corresponding number, $q_{ki}(\boldsymbol{r})$ is a monomial expression of coordinates x, y, z and a constant, m is the number of the primary term ($m = 4$ by default), and a_{ki} and b_{kj} are the unknown coefficients of the quadratic term and the primary term, respectively.

The global–local radial basis interpolation in Eqs. (9) and (10) can be further simplified as follows:

$$P(\boldsymbol{r}) = \sum_{i=1}^{n_t} N_i(\boldsymbol{r}) \cdot P_i, \quad (11)$$

where n_t is the total number of control points in Ω, $N_i(\boldsymbol{r})$ is the corresponding computable coefficient function and $\{P_i\}_{i=1}^{n_t}$ are the unknown design variables at the control points.

For clarity, a two-dimensional example of the global–local interpolation is illustrated in Fig. 4 (left). Given n control points,

the global radial basis interpolation needs to calculate a dense matrix with a size of $n \times n$. At the same time, the local radial basis interpolation needs to calculate a sparse matrix with a size of $n \times n$ with a certain bandwidth. Take an example, the design domain is divided into four sub-domains, we only need to calculate four small dense matrices, then, combining the four matrices by weights. Especially for large models with plenty of control points, the global–local radial basis interpolation only needs to calculate a few small matrices efficiently. Also, the global–local interpolation method is insensitive to the control point density of the sub-domains, and can easily modify the function values of the control points locally. The proposed global–local interpolation can improve computational efficiency, while making the structures have smooth changes, as illustrated in Fig. 4 (right).

4.2.2. Discrete form

In discrete form, a super element technique [45] is adopted to obtain an efficient calculation, while retaining a sufficient computational accuracy. Specifically, the 3D bounding box of a design domain is first divided into evenly hexahedral finite elements, called super elements. The super elements are used to generate the temperature field, and the number of super elements n_s is determined by the volume of the bounding box (10^3 super elements in a unit volume by default). Then, each super element is further subdivided into smaller hexahedral elements, called background elements. The background elements are used to perform more precise geometric calculations. Here, the number of background elements n_b in each super element is set to 27 by default. As shown in Fig. 5, the accuracy of our method in terms of the Max-Temperature and the Thermal Compliance is comparable to the commercial software: COMSOL Multiphysics, which is calculated by the finite element analysis. Moreover, the proposed porous structures are represented using functions, which avoids repeated remeshing during the optimization. The simple finite elements are used for integral calculation, hence, they only need to be constructed once in the optimization.

The discrete form of the heat conduction formulation in Eq. (7) can be expressed as follows:

$$\min_{P(\boldsymbol{r}), W(\boldsymbol{r})} C = \tilde{\boldsymbol{Q}}^T \boldsymbol{T} \quad (12)$$

s.t.

$$\boldsymbol{K}\boldsymbol{T} = \tilde{\boldsymbol{Q}},$$

$$V = \frac{1}{8} \sum_{i=1}^{N_b} \sum_{l=1}^{8} H_\eta \left(\Phi_l^i \right) v_b \leq \bar{v},$$

$$\mathcal{G} = \frac{1}{\|\Omega\|} \sum_{i=1}^{n_l} \mathcal{L} \left(\frac{\left(\frac{1}{N_b^i} \sum_{j=1}^{N_b^i} \left\| \nabla P_j^i \right\|^p \right)^{\frac{1}{p}}}{\bar{g}_i} - 1 \right) v_{\Omega_i} \leq 0,$$

where $\boldsymbol{T}$ is the vector of temperatures, $\tilde{\boldsymbol{Q}}$ is the vector of the heat source and heat flux term, $\boldsymbol{K}$ is a stiffness matrix, $N_b = n_b \times n_s$ is the total number of the background elements, $\|\Omega\|$ is the volume of Ω, N_b^i is the number of the background elements in the ith sub-domain Ω_i, v_b is the volume of a background element, ∇P_j^i is the gradient of $P(\boldsymbol{r})$ of the jth background element in the ith sub-domain Ω_i, v_{Ω_i} is the volume of the ith sub-domain Ω_i, $p > 0$ is a penalty factor of the global gradient constraint, and

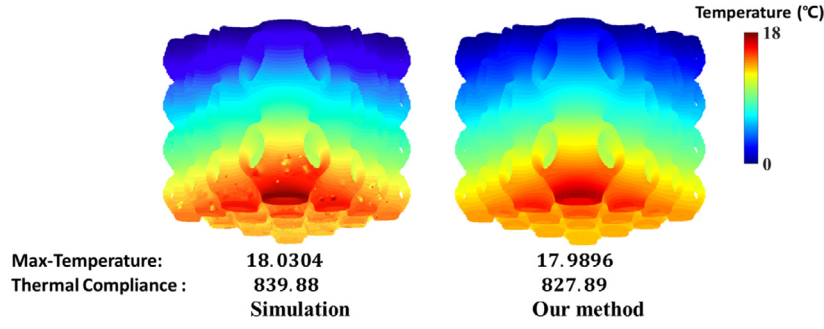$$\mathcal{L}(x) = \begin{cases} x^2, & \text{if } x \geq 0, \\ 0, & \text{if } x < 0. \end{cases} \quad (13)$$

Fig. 5. Accuracy comparison (temperature with a uniform colormap) between commercial software: COMSOL Multiphysics (left) and our method (right) under the same thermal source and constraint conditions (0.3 W/cm^2 is applied on the bottom with a fixed temperature on the top).
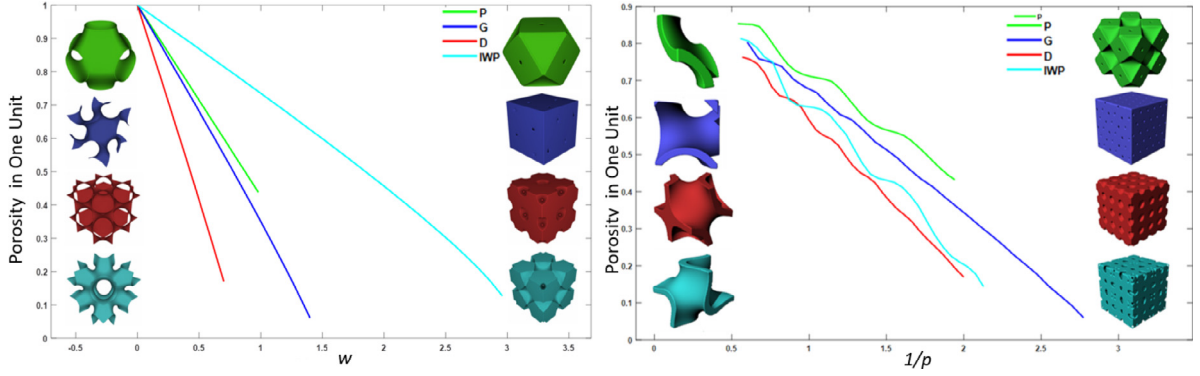

Fig. 6. Illustration of the parameter functions $W(\boldsymbol{r}) \equiv w$ and $P(\boldsymbol{r}) \equiv p$ for different types of TPMS-based porous structures. Variations of porosity in one unit are demonstrated for w (left) and $1/p$ (right).

5. Sensitive analysis and optimization

Optimization of the proposed 3D heat dissipation consists of two parts, period optimization and wall-thickness optimization. The period and thickness of the proposed TPMS-based porous structures are independently controlled by the period function $P(\boldsymbol{r})$ and the wall-thickness function $W(\boldsymbol{r})$, respectively. The Method of Moving Asymptotes (MMA) [46] is selected to solve the design variables of the two-step optimization processes. Theoretically, the two functions can be optimized simultaneously. However, since the choice strategy of moving asymptotes affects the convergence speed of the MMA optimizer [47], the common asymptotes cannot guarantee the convergence efficiency for both period and wall-thickness. Therefore, the simultaneous optimization strategy will lead to a slow convergence. To accelerate the optimization efficiency, we split the optimization into two sub-optimizations. Each sub-optimization is responsible for one function by fixing another one. Although the mathematical model of thermal dissipation problem is non-concave and its convergence cannot be proved [48], many experiments have confirmed the well numerical performance of MMA even for the non-concave problems. In our experiments, we cannot prove the convergence or anything concerning about the approximation of optimized result. But the convergence of the two functions can be achieved due to the monotonous regularity, which means that the period parameters and wall thickness parameters have a monotonic effect on the maximum temperature and volume ratio when one of them is fixed, as shown in Fig. 7. Also, the period optimization and wall-thickness optimization in all our experiments have achieved the termination criterion of convergence. The termination criteria is set as $\frac{\|C_i - C_i^{avg}\|}{C_i^{avg}} \leq 1 \times 10^{-4}$, $\frac{\|V_i - V_i^{avg}\|}{V_i^{avg}} \leq 1 \times 10^{-4}$,

and $V \leq \bar{v}$, $i = 11, 12, 13, \ldots$, where C_i and V_i are the thermal compliance and volume in the ith iteration, respectively, $\bar{v}$ is the upper bound of the volume, C_i^{avg} and V_i^{avg} are the average thermal compliance and volume in the last ten iterations, respectively. Moreover, the changes of the porous period (topological changes) are more vigorous than the wall-thickness. We first optimized the period function, which is considered a coarse adjustment on the structure. Then, the wall-thickness optimization was considered a fine adjustment. Different wall-thickness initializations have a small effect on the thermal compliance (the difference is less than 5% of the average compliance), if they are shifted around the mean value of available value ranges of $W(\boldsymbol{r})$. Furthermore, our experiments showed that both the compliance energy and the porous structures underwent few changes during the iteration between the period optimization and the wall-thickness optimization. Therefore, there is no need for iterative optimization between the two functions.

Period optimization. The period function $P(\boldsymbol{r})$ is constructed by radial basis interpolation on the control points (the variables $\{P_i\}_{i=1}^{n_t}$), and the sensitive analysis can be calculated as follows:

$$
\begin{aligned}
\frac{\partial C}{\partial P_i} &= -T^T \frac{\partial K}{\partial P_i} T \\
&= -\frac{1}{8} \sum_{k=1}^{n_s} T_k^T \left(\sum_{j=1}^{n_b} \frac{\partial \lambda_{kj}}{\partial \delta_{kj}} \sum_{l=1}^{8} \frac{\partial H_\eta \left(\Phi_l^{kj} \right)}{\partial P_i} \right) K^0 T_k,
\end{aligned}
\tag{14}
$$

$$
\frac{\partial V}{\partial P_i} = \frac{1}{8} \sum_{j=1}^{N_b} \sum_{l=1}^{8} \frac{\partial H_\eta \left(\Phi_l^j \right)}{\partial P_i} v_b,
\tag{15}
$$

$$\frac{\partial \mathcal{G}}{\partial P_i} = \frac{1}{\|\Omega\|} \sum_{j=1}^{n_l} \mathcal{L}'\left(\nabla G_j\right) \frac{\partial \nabla G_j}{\partial P_i} v_{\Omega_j}, \tag{16}$$

$$\frac{\partial \nabla G_j}{\partial P_i} = \frac{1}{N_b^j \bar{g}_j} \left(\frac{1}{N_b^j}\|\nabla P_s^j\|^p\right)^{\frac{1}{p}-1} \sum_{s=1}^{N_b^j} \|\nabla P_s^j\|^{p-1} \frac{\partial \|\nabla P_s^j\|}{\partial P_i},$$

where λ_{kj} and δ_{kj} mean the material thermal conductivity and the volume ratio of solid material of the jth background element in the kth super element, respectively, Φ_l^{kj} means the lth node point of the jth background element in the kth super element and K^0 is the initial stiffness matrix. The optimized porous structures with smooth period changes can be obtained by taking $\partial C/\partial P_i$, $\partial V/\partial P_i$ and $\partial \mathcal{G}/\partial P_i$ in the MMA optimizer. Since the wall-thickness function $W(\boldsymbol{r})$ should be fixed and the structure porosity monotonously increases with the increase of the period function $P(\boldsymbol{r})$, the convergence of period optimization is easy to achieve. In our experiments, the period optimization converged within 70 iterations.

Wall-thickness optimization. Similarly, the wall-thickness function $W(\boldsymbol{r})$ is also constructed by radial basis interpolation on the control points (the variables $\{W_i\}_{i=1}^{n_t}$, and the corresponding sensitive analysis can be calculated as follows:

$$\frac{\partial C}{\partial W_i} = -T^T \frac{\partial K}{\partial W_i} T \tag{17}$$

$$= -\frac{1}{8} \sum_{k=1}^{n_s} T_k^T \left(\sum_{j=1}^{n_b} \frac{\partial \lambda_{kj}}{\partial \delta_{kj}} \sum_{l=1}^{8} \frac{\partial H_\eta\left(\Phi_l^{kj}\right)}{\partial P_i}\right) K^0 T_k, \tag{18}$$

$$\frac{\partial V}{\partial W_i} = \frac{1}{8} \sum_{j=1}^{N_b} \sum_{l=1}^{8} \frac{\partial H_\eta\left(\Phi_l^j\right)}{\partial W_i} v_b. \tag{19}$$

Since the wall-thickness changes are smoother than period changes, the gradient constraint of $W(\boldsymbol{r})$ is no longer needed. Finally, the optimized porous structures with both smooth period and wall-thickness changes can be obtained by taking $\partial C/\partial W_i$ and $\partial V/\partial W_i$ in the MMA optimizer. Since the optimized period function $P(\boldsymbol{r})$ is fixed and the structure porosity monotonously increases with increasing of wall-thickness function $W(\boldsymbol{r})$, the convergence of wall-thickness optimization is also easy to achieve. In our experiments, the wall-thickness optimization converged within 30 iterations.

6. Experiments and discussions

This section describes the performances of the proposed optimized porous structures for heat dissipation that were demonstrated in various conditions. All the experiments were conducted on a 3.4 GHz Intel(R) Core(TM) i7 computer with 64G memory. The models in our experiment were P-TPMS-based porous structures that were set to $25 * 25 * 30$ cm^3 by default except where noted. The material of the porous shell structures was set as aluminum by default, whose thermal conductivity was 237 W/(m K). The heat sources (red parts) in the design domain were as follow: (1) the internal heat flux was set to 5 W/cm^3 (size: $3 * 3 * 3$cm^3 by default); (2) the inputting surface heat flux was set to 1 W/cm^2 (size: $6 * 6$ cm^2 by default). The cooling areas (blue parts) are Dirichlet boundary conditions that were set to a fixed temperature 0 °C (degree Celsius) by default, and their sizes were set to the same as the corresponding heat sources by default. The volume constraint was set to 20% of the corresponding solid model (bounding box) by default. To ensure that the study was like an actual situation, air was filled into the void with thermal conductivity as 0.001 W/(m K), and the other external sides were heat adiabatic in the design space.

Parameter functions. To better understand the TPMS-based porous structures, the effect of parameter functions $W(\boldsymbol{r})$ and $P(\boldsymbol{r})$ on different types of porous structures are illustrated in Fig. 6. Variations of porosity in one unit were locally observed, and the parameter functions $W(\boldsymbol{r}) \equiv w$ and $P(\boldsymbol{r}) \equiv p$ were set to be constant values. The local porosity variation in one unit can be considered to be part of the global material distribution, which is important to the heat dissipation. An optimized porosity variation can dramatically enhance structural cooling performance. As shown on the top of Fig. 6, for the wall-thickness parameter function $W(\boldsymbol{r})$, the porosity variations of different TPMS-based porous structures are monotonic declined with some differences. The porous structures degenerate into surfaces when $w = 0$ (as shown in the left part), and the structures will become solid models when w is beyond its value range (as shown in the right part). The value ranges of $W(\boldsymbol{r})$ are inconsistent for different types of porous structures. Generally, the value ranges are empirically set, such as $W(\boldsymbol{r}) \in [0.02, 0.95]$ for P-TPMS-based porous structures, $W(\boldsymbol{r}) \in [0.02, 1.35]$ for G-TPMS-based porous structures, $W(\boldsymbol{r}) \in [0.02, 0.7]$ for D-TPMS-based porous structures and $W(\boldsymbol{r}) \in [0.02, 2.95]$ for IWP-TPMS-based porous structures, respectively. Similarly, the influence of the period parameter function $P(\boldsymbol{r})$ is illustrated in bottom of Fig. 6. Its inverse of $1/P(\boldsymbol{r})$ can be analyzed for comparison. As $1/p$ increases, the porous structures periodically become denser, and turn into solid models when $1/p$ is larger than its value range. The value ranges of $P(\boldsymbol{r})$ are also inconsistent for different types of porous structures. Similarly, the value ranges of $1/P(\boldsymbol{r})$ are empirically set, such as $1/P(\boldsymbol{r}) \in [0.5, 2]$ for P-TPMS-based porous structures, $1/P(\boldsymbol{r}) \in [0.5, 2.7]$ for G-TPMS-based porous structures, $1/P(\boldsymbol{r}) \in [0.5, 2]$ for D-TPMS-based porous structures and $1/P(\boldsymbol{r}) \in [0.5, 2]$ for IWP-TPMS-based porous structures, respectively. This also illustrates that different types of TPMS-based porous structures can have similar performances on heat dissipation, and our subsequent experiments also demonstrated the performances. Moreover, we also illustrated the effect of the two parameter on some physical properties. As shown in Fig. 7, under the same loading conditions (model size: $25 * 25 * 25$ cm^3, bottom heat source size: $0.6 * 0.6$ cm^2, cooling area: top surface), the period parameters and wall-thickness parameters have monotonic effect on the maximum temperature and the volume ratio. The period optimization is considered to be a coarse adjustment on the structure while the wall-thickness optimization is considered a fine adjustment on the structure. Generally, the proposed optimization can converge to an optimized solution within total a hundred of iterations. In all the experiments, the period optimization converged within 70 iterations, while the wall-thickness optimization converged within 30 iterations. Table 1 lists the time analysis and comparison for the porous optimization. The results indicate that our optimization is effective due to the direct optimization on functions without remeshing.

Influence of the heat source and cooling area. To verify the effectiveness of the proposed porous structures, several examples can be illustrated with different heat sources and cooling areas. As shown in Fig. 8, different initial settings of heat sources and cooling areas are given, and cases of symmetry, asymmetry, and center-to-corners are shown from left to right, respectively. Both 3D optimized porous structures and the corresponding 2D cross-sections with the temperature distribution are demonstrated. As shown, the optimized structures automatically built obvious heat conduction channels between the heat source and the cooling areas, with smaller periods and larger wall-thickness. This will improve the heat conduction efficiency and is consistent with experience and common sense. Furthermore, the impact of heat source and cooling area sizes are illustrated. Different sizes of
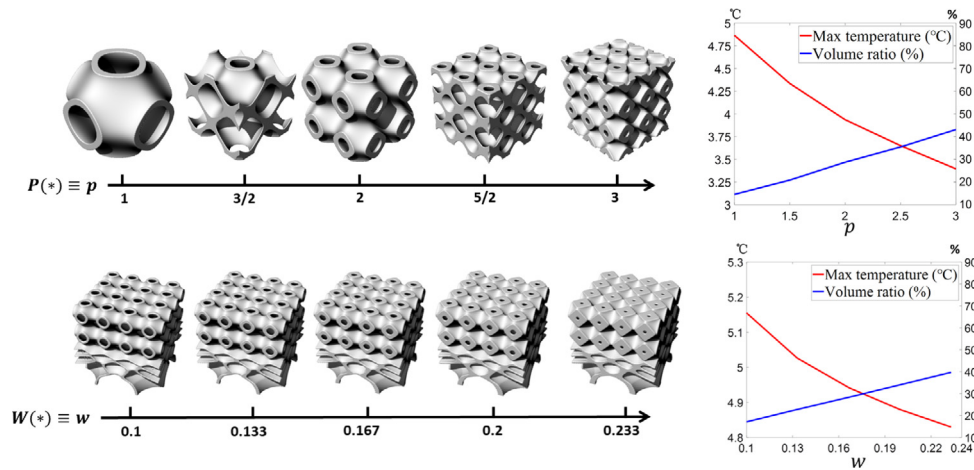
Fig. 7. Effect of the parameter functions $W(\mathbf{r}) \equiv w$ and $P(\mathbf{r}) \equiv p$ on the maximum temperature and volume ratio, respectively.
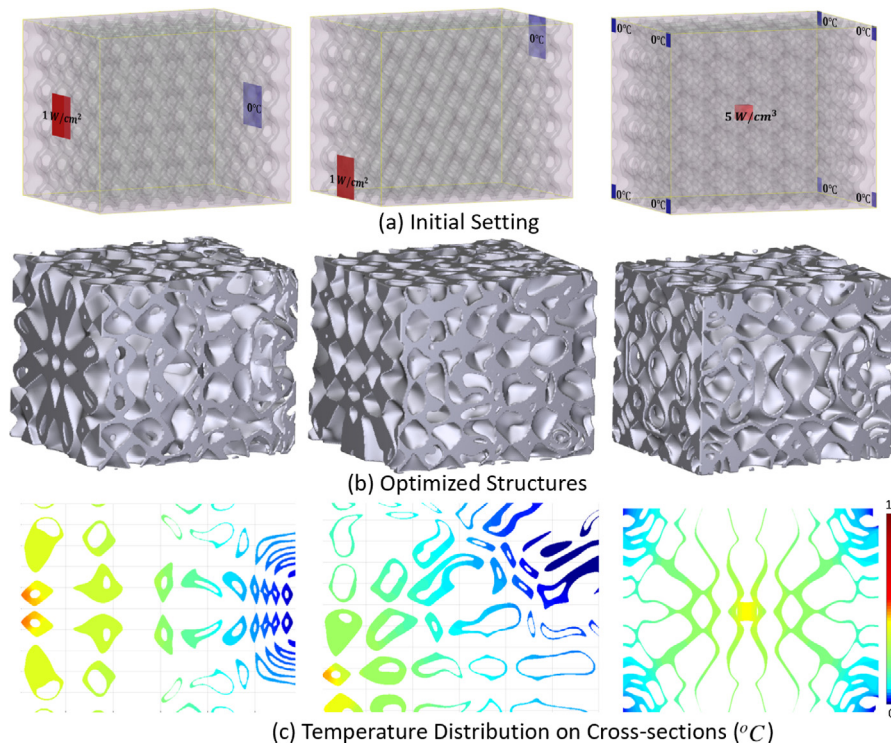

(a) Initial Setting

(b) Optimized Structures

(c) Temperature Distribution on Cross-sections (^{o}C)

Fig. 8. Illustration of the impact of heat source and cooling area positions. (a) Different initial settings of heat sources and cooling areas (symmetry, asymmetry, and center-to-corners). (b) Corresponding optimized porous structures. (c) Corresponding temperature distributions on 2D planes (middle face: y = 0 plane for the left two examples and x = 1.2y plane for the right one).

Table 1

Time analysis and comparison for the porous optimization. "Heating Size" means the size of the heat source, "♯Elements" means the number of background elements (the same resolution in FEM-based method), "P-Iteration" is the number of iterations for the period optimization, "W-Iteration" is the number of iterations for the wall-thickness optimization, "Our Time" and "FEM-Time" refer to the total optimization time (minutes) using our proposed method and FEM-based method (including remeshing), respectively.

Model Size (cm^3)	Heating Size (cm^2)	♯ Elements	Optimization		Our Time (m)	FEM-Time (m)
			P-Iteration	W-Iteration		
$25 \times 25 \times 30$	6×6	1.2×10^6	43	20	85.71	770.02
$25 \times 25 \times 30$	9×9	1.2×10^6	46	19	86.06	794.32
$25 \times 25 \times 30$	15×15	1.2×10^6	49	23	99.17	855.97
$25 \times 25 \times 20$	9×9	0.8×10^6	42	22	80.47	490.42
$30 \times 30 \times 9$	3×3	2.4×10^6	56	28	156.01	1912.48

heat sources and the corresponding cooling areas are demonstrated in Fig. 9, from left to right, show the sizes are 3∗3 cm^2, 9∗ 9 cm^2 and 15∗15 cm^2, respectively. Similarly, both 3D optimized porous structures and the corresponding 2D cross-sections with
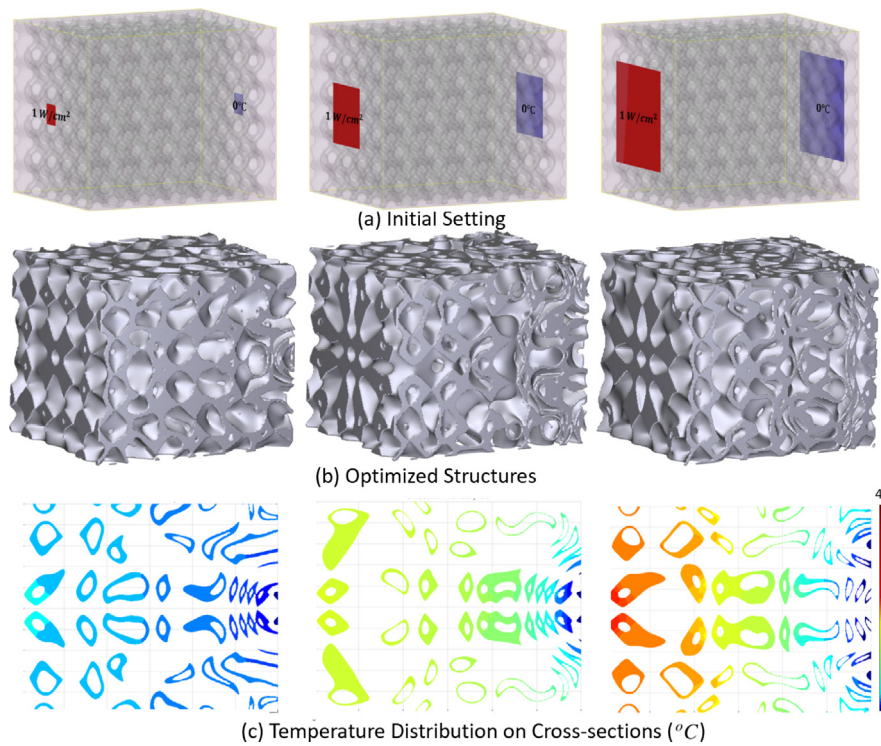
Fig. 9. Illustration of the impact of heat source and cooling area sizes. (a) Initial setting with different sizes of heat sources and cooling areas (from left to right: $3*3$ cm^2, $9*9$ cm^2 and $15*15$ cm^2, respectively). (b) Corresponding optimized porous structures. (c) Corresponding temperature distributions in the 2D plane (middle face: y = 0 plane).
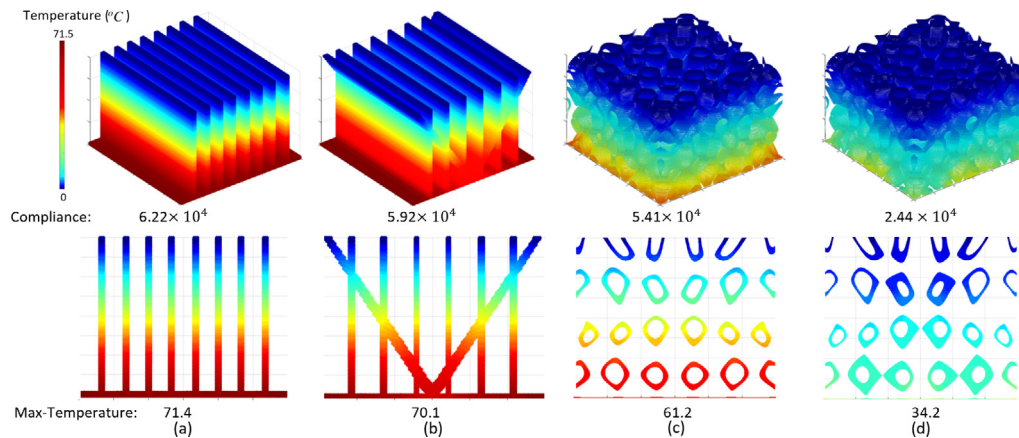

Fig. 10. Comparing with two kinds of traditional heat sink structures under the same initial conditions (size: $20*30*30$ cm^3, volume constraint: 20% of the solid model and heat source size: $30*30$ cm^2). (a) General plug heat sink structure and its temperature distribution in 2D (middle face: y = 0 plane). (b) Heat sink structure with a V-shape branch and the corresponding temperature distribution. (c) Our TPMS-based porous structure with only period optimization and the corresponding temperature distribution. (d) Our porous structure with both optimized period and wall-thickness. Our optimized porous structures have higher thermal efficiency (lower compliance and max-temperature of the structures), even when there is only period optimization.

the temperature distribution are illustrated. As the heat source size increases, the wall-thickness near the heat source increases markedly, which can be concluded from Table 2. To achieve a high heat conduction efficiency, there is also a tradeoff between the period and wall-thickness under the given volume constraint. Moreover, these examples demonstrate that the changes in the period and wall-thickness of the optimized structures are smooth and natural. This is an important factor that will be beneficial to structural stress and manufacturing, which we will investigate in further work.

Comparison with traditional heat dissipation structures. To prove the validity of the proposed method, we compared our optimized porous structures with traditional heat sink structures,

such as a plug heat sink structure and a V-shape heat sink structure, as shown in Fig. 10. For ease of comparison, all the structures had the same volume constraints (20% of the solid model), the same size heat sources ($30*30$ cm^2), and the same average wall-thickness (Fig. 10(a), (b) and (c)). The proposed optimized porous structures had a higher heat-conducting efficiency (lower compliance and max-temperature of the structures), even when there was only period optimization (Fig. 10(c)). The wall-thickness optimization further enhanced the efficiency of thermal conduction.

Comparison with lattice structures. Moreover, the optimized structure was compared with a 3D lattice structure proposed in [3]

Table 2

Comparison of the average wall-thickness of models with different heat source size. "Heating Size" means the size of the heat source, "Average wall thickness" can be obtained by dividing the volume by the surface area of the specified cross-section, "♯L-Section" means the left cross-section near the heat source, "♯M-Section" means the middle cross-section, and "♯R-Section" means the right cross-section.

Model Size (cm³)	Heating Size (cm³)	Average wall thickness (cm)		
		♯L-Section	♯M-Section	♯R-Section
$25 \times 25 \times 30$	3×3	0.486	0.403	0.283
$25 \times 25 \times 30$	9×9	0.498	0.361	0.260
$25 \times 25 \times 30$	15×15	0.518	0.350	0.250

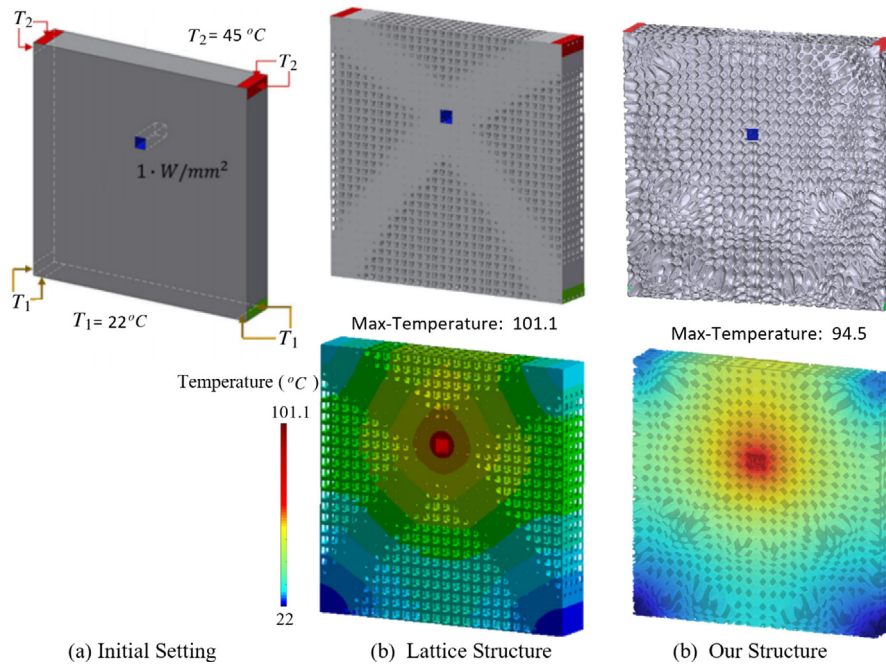(a) Initial Setting (b) Lattice Structure (b) Our Structure

Fig. 11. A Comparison between 3D lattice structure and our structure under the same conditions. (a) The initial setting (volume constraint: 50%; heat source (blue): 1 W/mm²; cooling areas: red (45 °C), green (22 °C)). (b) The optimized lattice structure in [3]. (c) Our optimized TPMS-based porous structure. Our optimized porous structure has a better thermal efficiency than the lattice structure in term of the maximum temperature. (For interpretation of the references to color in this figure legend, the reader is referred to the web version of this article.)
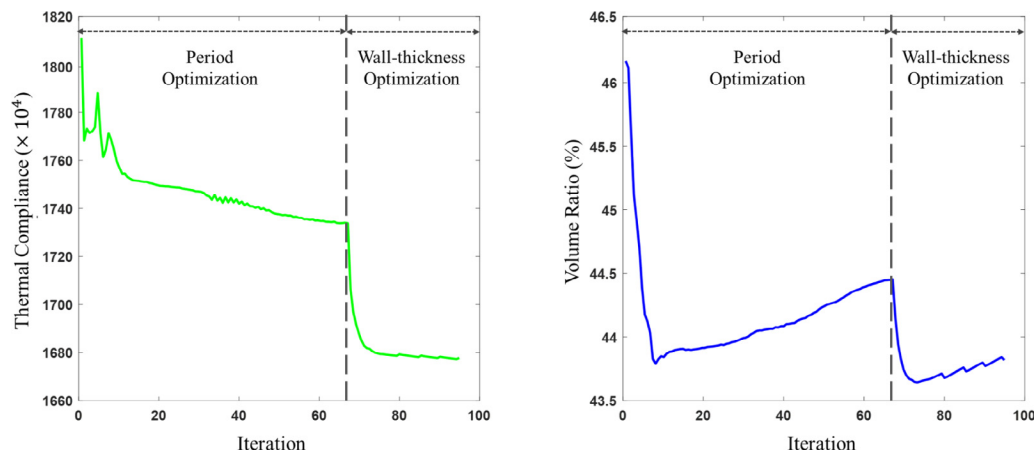

Fig. 12. Illustration of the optimization iteration curves, including the thermal compliance curve (left) and the volume curve (right).

under the same conditions, as shown in Fig. 11. The optimized lattice structure in [3] had a higher maximum temperature 101.1 °C, and the maximum temperature of the proposed porous structure was 94.5 °C. Moreover, the optimized thermal compliance of the lattice structure in [3] is 1.756×10^8 W K, and the optimized thermal compliance in Eq. (7) decreases from 1.811×10^8 W K to 1.679×10^8 W K (7.3% decrease). The smaller the thermal compliance, the higher the efficiency of thermal conductivity. Our optimized TPMS-based porous structure had better thermal efficiency than the lattice structure in terms of the maximum temperature and the thermal compliance. Since both methods were executed without remeshing, the optimizations were efficient and the computational time was comparable. The proposed
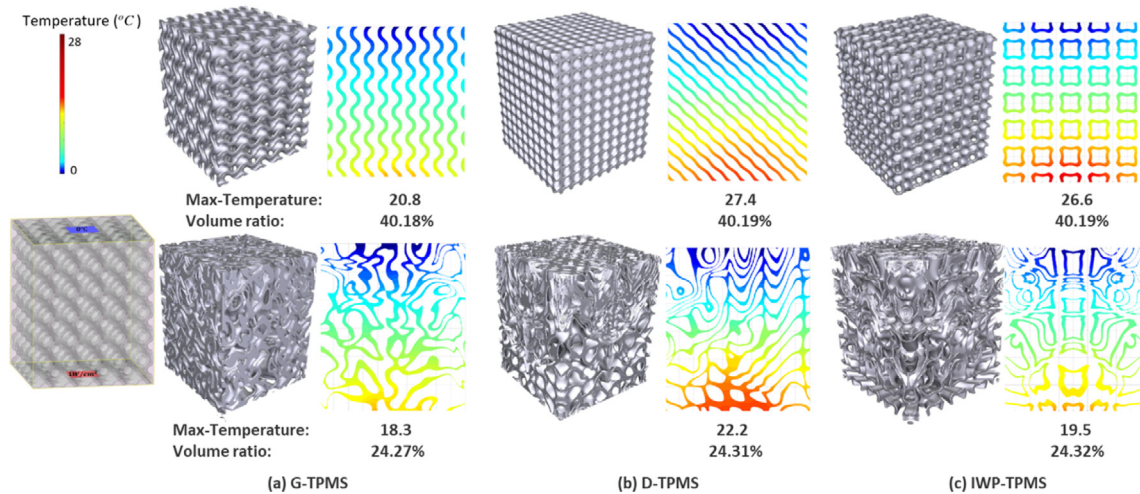
Fig. 13. A Comparison of different types of TPMS-based porous structures under the same conditions. (a) The optimized G-TPMS-based porous structure and the temperature distribution in 2D (y = 0, XZ plane). (b) The optimized D-TPMS-based porous structure and the corresponding temperature distribution. (c) The optimized IWP-TPMS-based porous structure and the corresponding temperature distribution.

Table 3
Comparison of porous optimizations with different initial parameters. The "initial parameter", "$P(r) \equiv p$" and "$W(r) \equiv w$" mean consistent initial values of the periodic parameter function and the wall-thickness parameter function, respectively. "Initial Value" and "Optimized Value" are the values before and after optimization, respectively. "Iteration" is the total iteration of optimization.

Initial parameters		Initial Value		Optimized Value		Iteration
$P(r) \equiv p$	$W(r) \equiv w$	Thermal compliance $(W \cdot K)$	Volume ratio (%)	Thermal compliance $(W \cdot K)$	Volume ratio (%)	
1.8	0.82	1.766×10^8	48.96	1.637×10^8	43.71	84
1.4	0.82	1.811×10^8	46.33	1.679×10^8	43.63	93
1.4	0.64	2.242×10^8	37.03	1.75×10^8	40.08	95
1	0.48	2.905×10^8	28.54	1.749×10^8	39.64	99

TPMS-based porous structures were obtained by directly optimizing both topology and geometry (wall-thickness). However, the mapping method used to construct lattice structures in [3] may cause some drawbacks. First, the mapping of density distribution is inconsistent in local density distribution, which will lead to a deviation of heat dissipation between the density distribution and the actual lattice structure. Second, there must be a certain material distribution in each unit, and it will lead to a waste of material in the unimportant area for heat conduction. Finally, the material alignment between adjacent lattices is difficult due to the uniform parameter variables, and the continuity and smoothness of structures are difficult to be controlled directly by density mapping. Therefore, the accuracy and controllability of the lattice structures seemed deficient, and the lack of smoothness will also affect the heat dissipation and 3D printing. Moreover, the optimization convergence of the proposed method is also illustrated in Fig. 12. We can see that the period optimization converged after 67 iterations, and the wall-thickness optimization converged after 28 iterations. Finally, we obtained the optimized TPMS-based porous structures within 100 iterations. In the processes of period optimization the volume first decreased rapidly, then increased to achieve a decline of heat compliance. There are two local peaks of heat compliance in the initial period optimization, because the topology is sensitive to the variables. In the period optimization, both the volume and heat compliance decreased steadily until they converge. The convergence curves also verify the rationality of the optimization, in which the period optimization is treated to be a coarse adjustment while the wall-thickness optimization is treated to be a fine adjustment.

In order to better understand our structures, we also show more optimized results with different initial parameters. As listed in Table 3, the results of porous optimization with different initial parameters were compared under the same conditions (design domain, heat source and heat dissipation surface).

Comparison of different types of TPMS-based porous structures. A performance comparison of different types of TPMS-based porous structures (G-TPMS, D-TPMS and IWP-TPMS) was also conducted in Fig. 13. The first row shows the original TPMS-based porous structures and their temperature distributions in a 2D plane (middle face: y = 0 plane). The second row shows the corresponding optimized TPMS-based porous structures and their temperature distributions. As shown, the maximum temperatures (degree Celsius) of the initial TPMS-based porous structures were 20.8 °C, 27.4 °C and 26.6 °C, respectively, and the maximum temperatures (degree Celsius) of the optimized TPMS-based porous structures were 18.3 °C, 22.2 °C and 19.5 °C, respectively. Due to the structural similarity, there was little difference in heat dissipation among the three types of TPMS-based porous structures. However, the optimized porous structures had certain improvements in thermal conduction efficiency relative to the initial TPMS-based porous structures. For example, the performance of the IWP-TPMS-based porous structure improved by as much as 26.7% in terms of the maximum temperature.

Limitations. Although the proposed optimization of TPMS-based porous structures is more efficient than traditional FEM-based computation, the solution accuracy is determined by the background elements (calculation of integral in the discrete form). Both the FEM-based method and the meshless method suffer from the same problem. We will continue to investigate optimization to obtain a reasonable tradeoff between efficiency and accuracy. Moreover, in this study, we focused on the problem of steady-state heat conduction with a single material and simple conditions. To further promote the heat-conducting efficiency, we would like to extend our framework to heat dissipation under forced convection conditions and the problem of fluid heat transfer [49] in the future.

7. Conclusions

In this paper, an efficient optimization method is proposed for TPMS-based porous shell structures for heat dissipation. The proposed porous structures with function representations inherit good properties, such as full connectivity, good controllability, high surface-to-volume ratio, high smoothness, and good mechanical property. By applying the proposed porous structures to 3D heat dissipation, an optimized porous structure with continuous geometry changes and smooth topology changes is obtained. Compared with existing traditional heat sink structures, the proposed porous structures substantially improve the efficiency and effectiveness of thermal conduction. Various experimental results showed the effectiveness of the proposed method.

Declaration of competing interest

The authors declare that they have no known competing financial interests or personal relationships that could have appeared to influence the work reported in this paper.

Acknowledgments

Appendix

The equation in Eq. (6) can be rewritten into compliance energy by multiplying both sides with test function ω and calculate the integration over the design domain as follows:

$$\int_{\Omega} \lambda \nabla^2 T \omega d\Omega + \int_{\Omega} \omega^T Q d\Omega = \int_{\Omega} \rho C_p \frac{\partial T}{\partial t} \omega d\Omega = 0. \quad (A.1)$$

The above equation is equivalent to

$$-\int_{\Omega} \lambda \nabla T \nabla \omega d\Omega + \int_{\Omega} \lambda \nabla (\nabla T \omega) d\Omega + \int_{\Omega} \omega^T Q d\Omega = 0. \quad (A.2)$$

Then, we obtain the weak solution formulation:

$$\int_{\Omega} \lambda \nabla T \nabla \omega d\Omega = \oint_{\Gamma} \lambda \frac{\partial T}{\partial n} \omega d\Gamma \quad (A.3)$$

$$= \int_{\Gamma_Q} H(\Phi)\omega^T q_S d\Gamma + \int_{\Omega} \omega^T Q d\Omega$$

$$+ \int_{\Gamma_T} \lambda \nabla \bar{T} \omega d\Gamma.$$

The equation can be simply expressed as

$$a(\omega, T) = L(\omega) + B(\omega, \bar{T}), \quad (A.4)$$

where $a(\omega, T) = \int_{\Omega} \lambda \nabla T \nabla \omega d\Omega$, $L(\omega) = \int_{\Gamma_Q} H(\Phi)\omega^T q_S d\Gamma + \int_{\Omega} \omega^T Q d\Omega$, and $B(\omega, \bar{T}) = \int_{\Gamma_T} \lambda \nabla \bar{T} \omega d\Gamma$. Therefore, we obtain the formulation in Eq. (7).

References

[1] Chen Y, Zhou S, Li Q. Multiobjective topology optimization for finite periodic structures. Comput Struct 2010;88(11–12):806–11.

[2] Burger FH, Dirker J, Meyer JP. Three-dimensional conductive heat transfer topology optimisation in a cubic domain for the volume-to-surface problem. Int J Heat Mass Transfer 2013;67:214–24.

[3] Cheng L, Liu J, To A. Concurrent lattice infill with feature evolution optimization for additive manufactured heat conduction design. Struct Multidisc Optim 2018;58:511–35.

[4] Li D, Dai N, Tang Y, Dong G, Zhao Y. Design and optimization of graded cellular structures with triply periodic level surface-based topological shapes. J Mech Des 2019;7(141):1–13.

[5] Elliott O, Gray S, McClay M, Nassief B, Nunnelley A, Vogt E, Ekong J, Kardel K, Khoshkhoo A, Proano G. Design and manufacturing of High Surface Area 3D-printed media for moving bed bioreactors for wastewater treatment. J Contemp Water Res Educ 2017;160(1):144–56.

[6] Al-Ketan O, Pelanconi M, Ortona A, Al-Rub RKA. Additive manufacturing of architected catalytic ceramic substrates based on triply periodic minimal surfaces. J Am Ceram Soc 2019;102(10):6176–93.

[7] Pouya C, Overvelde JT, Kolle M, Aizenberg J, Bertoldi K, Weaver JC, Vukusic P. Characterization of a mechanically tunable gyroid photonic crystal inspired by the butterfly parides sesostris. Adv Opt Mater 2016;4(1):99–105.

[8] Bendsøe M, Kikuchi N. Generating optimal topologies in structural design using a homogenization method. Comput Methods Appl Mech Engrg 1988;71(2):197–224.

[9] Fujii D, Chen B, Kikuchi N. Composite material design of two-dimensional structures using the homogenization design method. Internat J Numer Methods Engrg 2001;50(9):2031–51.

[10] Bendsøe M. Optimal shape design as a material distribution problem. Struct Optim 1989;1:193–202.

[11] Zhou M, Rozvany G. The COC algorithm, part II: Topological, geometrical and generalized shape optimization. Comput Methods Appl Mech Engrg 1991;89(1–3):197–224.

[12] Xie Y, Steven G. A simple evolutionary procedure for structural optimization. Comput Struct 1993;49(5):885–96.

[13] Xie Y, Steven G. Evolutionary structural optimization. Springer London; 1997.

[14] Bendsøe MP, Sigmund O. Extensions and applications. Springer Berlin Heidelberg; 2004.

[15] Gersborg-Hansen A, Bendsøe M, Sigmund O. Topology optimization of heat conduction problems using the finite volume method. Struct Multidiscip Optim 2006;31(4):251–9.

[16] Page LG, Dirker J, Meyer J. Topology optimization for the conduction cooling of a heat-generating volume with orthotropic material. Int J Heat Mass Transf 2016;103:1075–83.

[17] Lin Q, Hong J, Liu Z, Li B, Wang J. Investigation into the topology optimization for conductive heat transfer based on deep learning approach. Int Commun Heat Mass Transfer 2018;97:103–9.

[18] Gao T, Zhang W, Zhu J, Xu Y, Bassir D. Topology optimization of heat conduction problem involving design-dependent heat load effect. Finite Elem Anal Des 2008;44(14):805–13.

[19] Li Q, Steven GP, Xie Y, Querin OM. Evolutionary topology optimization for temperature reduction of heat conducting fields. Int J Heat Mass Transfer 2004;47(23):5071–83.

[20] Boichot R, Luo L, Fan Y. Tree-network structure generation for heat conduction by cellular automaton. Energy Convers Manage 2009;50(2):376–86.

[21] Cheng X, Li Z, Guo Z. Constructs of highly effective heat transport paths by bionic optimization. Sci China 2003;(3):296–302.

[22] Mei Y, Wang X. A level set method for structural topology optimization and its applications. Comput Methods Appl Mech Engrg 2004;35(7):415–41.

[23] Dijk N, Maute K, Langelaar M, Keulen F. Level-set methods for structural topology optimization. Struct Multidiscip Optim 2013;48(3):437–72.

[24] Bejan A. Constructal-theory network of conducting paths for cooling a heat generating volume. Int J Heat Mass Transfer 1997;40(4):799–816.

[25] Xu G, Zhang W, Zhong W. Doing topology optimization explicitly and geometrically—A new moving morphable components based framework. J Appl Mech 2014;81(8):081009.

[26] Yamada T, Yamasaki S, Nishiwaki S, Izui K, Yoshimura M. Structural optimization of compliant thermal micro-actuators based on the level set method. Trans Japan Soc Comput Eng Sci 2008:1–10.

[27] Zhuang CG, Xiong Z, Ding H. A level set method for topology optimization of heat conduction problem under multiple load cases. Comput Methods Appl Mech Engrg 2007;196(4–6):1074–84.

[28] Pizzolato A, Sharma A, Maute K, Sciacovelli A, Verda V. Multi-scale topology optimization of multi-material structures with controllable geometric complexity —Applications to heat transfer problems. Comput Methods Appl Mech Engrg 2019;357:112552.

[29] Dede E. Multiphysics topology optimization of heat transfer and fluid flow systems. In: COMSOL conference. At: Boston, MA; 2009.

[30] Alexandersen J, Aage N, Andreasen CS, Sigmund O. Topology optimisation for natural convection problems. Internat J Numer Methods Fluids 2014;76(10):699–721.

[31] Alexandersen J, Sigmund O, Aage N. Large scale three-dimensional topology optimisation of heat sinks cooled by natural convection. Int J Heat Mass Transfer 2016;100:876–91.

[32] Lohan DJ, Dede EM, Allison JT. Topology optimization for heat conduction using generative design algorithms. Struct Multidiscip Optim 2017;55(3):1063–77.

[33] Zhang W, Yuan J, Zhang J, Guo X. A new topology optimization approach based on moving morphable components (MMC) and the ersatz material model. Struct Multidiscip Optim 2016;53(6):1243–60.

[34] Cvijovi D, Klinowski J. The t and clp families of triply periodic minimal surfaces. J Physique 1992;12(2):137–47.

[35] Rajagopalan S, Robb RA. Schwarz meets schwann: Design and fabrication of biomorphic and durataxic tissue engineering scaffolds. Med Image Anal 2006;10(5):693–712.

[36] Melchels FPW, Bertoldi K, Gabbrielli R, Velders AH, Feijen J, Grijpma DW. Mathematically defined tissue engineering scaffold architectures prepared by stereolithography. Biomaterials 2010;31(27):6909–16.

[37] Yoo DJ. Porous scaffold design using the distance field and triply periodic minimal surface models. Biomaterials 2011;32(31):7741–54.

[38] Yoo DJ. Heterogeneous minimal surface porous scaffold design using the distance field and radial basis functions. Med Eng Phys 2012;34(5):625–39.

[39] Cai S, Xi J. A control approach for pore size distribution in the bone scaffold based on the hexahedral mesh refinement. Comput Aided Des 2008;40(10–11):1040–50.

[40] Yang N, Quan Z, Zhang D, Tian Y. Multi-morphology transition hybridization cad design of minimal surface porous structures for use in tissue engineering. Comput Aided Des 2014;56:11–21.

[41] Hu J, Wang S, Wang Y, Li F, Luo Z. A lightweight methodology of 3D printed objects utilizing multi-scale porous structures. Vis Comput 2019;35:949–59.

[42] Peng H, Gao F, Hu W. Design, modeling and characterization of triply periodic minimal surface heat exchangers with additive manufacturing. In: Solid Freeform Fabrication. 2019, p. 2325–37.

[43] Li M, Zhu L, Li J, Zhang K. Design optimization of interconnected porous structures using extended triply periodic minimal surfaces. Journal of Computational Physics 2021;425(15):109909.

[44] Ohtake Y, Belyaev A, Alexa M, Turk G, Seidel HP. Multi-level partition of unity implicits. ACM Trans Graph 2003;22(3):463–70.

[45] Nguyen TH, Paulino GH, Song J, Le CH. A computational paradigm for multiresolution topology optimization (mtop). Struct Multidiscip Optim 2010;41(4):525–39.

[46] Svanberg K. The method of moving asymptotes - A new method for structural optimization. Internat J Numer Methods Engrg 1987;24(2):359–73.

[47] Zillober C. A globally convergent version of the method of moving asymptotes. Struct Optim 1993;6(3):166–74.

[48] Zillober C. Eine global konvergente Methode zur Lösung von Problemen aus der Strukturoptimierung [Ph.D. thesis], Technische Universität München; 1992.

[49] Thomas, Navya, Sreedhar, Nurshaun, Al-Ketan, Oraib, Rowshan, Reza, Abu, Al-Rub. 3D printed triply periodic minimal surfaces as spacers for enhanced heat and mass transfer in membrane distillation. Desalination Int J Sci Technol Desalting Water Purif 2018;443:256–71.